IEEE Access
Multidisciplinary | Rapid Review | Open Access Journal

Received September 24, 2020, accepted October 8, 2020, date of publication October 12, 2020, date of current version October 21, 2020.

Digital Object Identifier 10.1109/ACCESS.2020.3030530

Probability Density Function of Three-Phase Ellipse Parameters for the Characterization of Noisy Voltage Sags

DIEGO BELLAN, (Member, IEEE)
Department of Electronics, Information and Bioengineering, Politecnico di Milano, 20133 Milan, Italy
e-mail: diego.bellan@polimi.it

ABSTRACT This work deals with the statistical analysis of additive noise impact on the space-vector ellipse parameters used to detect and classify three-phase voltage sags. In fact, since voltage waveforms are always corrupted by additive noise and harmonics, the space vector is pre-processed through the Discrete Fourier Transform to extract the power frequency components. Thus, harmonics can be readily discarded, but additive noise can still have significant impact on the elliptical trajectory of the space vector on the complex plane. Therefore, by modeling the ellipse parameters (i.e., the shape index and the inclination angle) as random variables, the related statistical characterization is derived in the paper. In particular, the main results and the novelty of the paper are given by the analytical derivation in closed-form of the probability density function, cumulative distribution function, mean value, and variance of the ellipse parameters as functions of the additive noise variance. Since the ellipse shape index and inclination angle are commonly used to detect and classify voltage sags, the results derived in the paper are useful for both uncertainty propagation analysis, and assessment of detection capability in case of voltage dips close to the minimum value defined in the IEEE Standard 1159. Analytical results are validated through numerical simulation of noisy voltage sags.

INDEX TERMS Additive noise effects, discrete Fourier transform, frequency-domain analysis, power quality, space vector ellipse, statistical analysis, voltage sags.

I. INTRODUCTION

A. MOTIVATION

Among all the power quality issues regarding three-phase power systems, voltage sags, also called voltage dips, represent a major concern together with supply interruptions [1], [2]. Indeed, according to the IEEE Standard 1159, a voltage sag is a decrease in the RMS voltage of 10-90% of the nominal value for durations from 0.5 cycles to 1 minute [3]. As the most frequent power quality disturbance, voltage sags can have severe consequences spanning from malfunctioning of control system equipment, to disconnection or loss of efficiency in electric machines. For this reason, many researchers have focused on the analysis, classification and characterization of voltage sags (e.g., [4]–[10]). Not much attention, however, has been devoted to measurement uncertainty due to the presence of harmonics and additive noise. Nevertheless, this point is crucial since harmonics and noise can affect proper classification and characterization of voltage sags.

The associate editor coordinating the review of this manuscript and approving it for publication was Arash Asrari.

B. LITERATURE REVIEW

One of the most effective techniques for real-time detection and classification of voltage sags is the space vector approach [11]–[20]. Indeed, starting from the pioneering work [11], the space vector approach has become popular for its straightforward geometrical properties. In fact, under normal operation, the power-frequency component (i.e., the 50/60 Hz component) of the space vector corresponding to balanced three-phase voltages describes a circular trajectory on the complex plane. When an unbalanced voltage sag occurs (i.e., when the voltage drop is not the same for all the phases), however, the space vector trajectory becomes elliptical [11]–[18]. In this case, the geometrical parameters of the ellipse, i.e., the semi-major axis, the semi-minor axis, and the inclination angle, allow a fast identification of the

type of voltage sag. In particular, the ratio between the ellipse axes (i.e., the so-called shape index) detects the onset of an unbalanced voltage sag, whereas the ellipse inclination angle identifies the dropped phases in both single-phase and double-phase dips. An interesting generalization was proposed in [19], [20] where a 3-D polarization ellipse was introduced. The five parameters of the 3-D ellipse were exploited for both classification and localization of fault voltage sags.

C. CONTRIBUTION AND PAPER ORGANIZATION

As pointed out in several papers, the main drawback of the space vector approach is that the space vector is normally corrupted by additive noise and harmonics [11], [14]. In fact, the ellipse mentioned above is related to the power-frequency component only. Thus, the space vector must be properly preprocessed in order to extract relevant information at power frequency. This can be readily accomplished through the Discrete Fourier Transform (DFT) which allows efficient evaluation of the space vector spectrum. Notice that other interesting transforms could be used for extraction of relevant information from noisy and distorted space vectors (e.g., orthogonal polynomials in [21], [22]). However, the derivations proposed in this paper are based on the DFT for two main reasons. First, the DFT is a common and well-known tool within the context of power system analysis. Second, in Section II it will be shown that the statistical effects of additive noise on DFT coefficients is already a well-known issue in the relevant literature. Thus, while harmonics can be effectively discarded through the DFT, the impact of additive noise at power frequency can be still significant. This is a crucial point since additive noise at power frequency affects the estimates of the ellipse parameters for voltage sag detection and classification. Despite this issue was pointed out in several papers, a specific analytical investigation of additive noise effects on ellipse parameters is still missing in the relevant literature. Therefore, the statistical analysis of additive noise effects on ellipse parameters for voltage sag detection and classification is the main objective of this work. Possible impact of multiplicative noise is not investigated in this paper.

In particular, the main contribution of this paper is the analytical derivation of the probability density function, cumulative distribution function, mean value, and variance of the ellipse parameters as functions of the additive noise level. The importance of the presented results is twofold. First, complete uncertainty analysis of the ellipse parameters allows proper classification of voltage sags by improving the decision-making process. Second, the impact of additive noise on detection of voltage sags is described in probabilistic terms.

The paper is organized as follows. In Section II the main properties of the DFT of a noisy and distorted space vector are described. In Section III the ellipse parameters for voltage sag detection and classification are defined in terms of the power-frequency DFT coefficients of the space vector. In Section IV the statistical analysis of the additive noise impact on ellipse parameters is presented. In particular, the statistical properties of the ellipse shape index and inclination angle are derived in closed form. In Section V the analytical results are validated through numerical simulations of noisy space vectors with elliptical trajectory, whereas in Section VI real data recorded by DOE/EPRI are used for further validation. Finally, the main results of the paper are summarized and discussed in Section VII.

II. FOURIER ANALYSIS OF VOLTAGE SPACE VECTOR

Space vector definition is based on the time-domain Clarke transformation of the phase variables in a three-phase circuit. The Clarke transformation $\left[v_\alpha v_\beta v_0\right]^T$ of the phase voltages $[v_a v_b v_c]^T$ is given by [23]:

$$\begin{bmatrix} v_\alpha \\ v_\beta \\ v_0 \end{bmatrix} = \boldsymbol{T} \begin{bmatrix} v_a \\ v_b \\ v_c \end{bmatrix} = \sqrt{\frac{2}{3}} \begin{bmatrix} 1 & -1/2 & -1/2 \\ 0 & \sqrt{3}/2 & -\sqrt{3}/2 \\ 1/\sqrt{2} & 1/\sqrt{2} & 1/\sqrt{2} \end{bmatrix} \begin{bmatrix} v_a \\ v_b \\ v_c \end{bmatrix} \quad (1)$$

where $\boldsymbol{T}$ is an orthogonal matrix, i.e., $\boldsymbol{T}^{-1} = \boldsymbol{T}^t$.

The corresponding space vector is defined as the complex-valued time-domain function given by [24], [25]:

$$\bar{v}(t) = v_\alpha(t) + j v_\beta(t) = \sqrt{\frac{2}{3}} \left(v_a + a v_b + a^2 v_c \right) \quad (2)$$

where $a = e^{j2\pi/3}$.

Under sinusoidal steady-state conditions with angular frequency ω_0 it can be shown that the space vector can be written as:

$$\bar{v}(t) = V_p e^{j\omega_0 t} + V_n^* e^{-j\omega_0 t} \quad (3)$$

where V_p and V_n^* are the positive-sequence and the negative-sequence (complex conjugate) phasors, according to the well-known symmetrical component transformation [26]:

$$\begin{bmatrix} V_p \\ V_n \\ V_0 \end{bmatrix} = \boldsymbol{S} \begin{bmatrix} V_a \\ V_b \\ V_c \end{bmatrix} = \frac{1}{\sqrt{3}} \begin{bmatrix} 1 & a & a^2 \\ 1 & a^2 & a \\ 1 & 1 & 1 \end{bmatrix} \begin{bmatrix} V_a \\ V_b \\ V_c \end{bmatrix} \quad (4)$$

where $\boldsymbol{S}$ is a unitary matrix, i.e., $\boldsymbol{S}^{-1} = \boldsymbol{S}^{*t}$.

Notice that (3) can be advantageously interpreted as a double decomposition of the space vector, i.e., the positive/negative-sequence decomposition, and the frequency decomposition in two spectral lines located in $\pm\omega_0$. Thus, V_p and V_n^* can be seen as the complex Fourier coefficients corresponding to the sinusoidal steady-state, i.e., $V_1 = V_p$ and $V_{-1} = V_n^*$. Contrary to the case of real-valued time-domain functions, however, the two Fourier coefficients corresponding to $\pm\omega_0$ are not related each other by complex conjugation (i.e., $V_{-1} \neq V_1^*$). In fact, since the space vector is a complex-valued function the two Fourier coefficients $V_1 = V_p$ and $V_{-1} = V_n^*$, corresponding to $\pm\omega_0$, are independent each other.

According to the interpretation mentioned above, in the more general case of distorted steady-state conditions the space vector can be written in the complex series form [27]:

$$\bar{v}(t) = \sum_{k=-\infty}^{+\infty} V_k e^{jk\omega_0 t} \tag{5}$$

where V_k and V_{-k} are the positive-sequence and negative-sequence (complex conjugate) phasors at $k\omega_0$, respectively.

It can be readily shown that the complex coefficients in (5) are given by:

$$V_k = \frac{1}{T}\int_0^T \bar{v}(t) e^{-jk\omega_0 t} dt \tag{6}$$

where $T = 2\pi/\omega_0 = 1/f_0$.

The complex coefficients (6) can be evaluated through the well-known Discrete Fourier Transform (DFT) of the space vector samples. By taking N_s samples in one period of $\bar{v}(t)$ (i.e., $N_s T_s = T$ where $T_s = 1/f_s$ is the sampling interval), the complex coefficients (6) are given by:

$$V_k = \frac{1}{N_s} DFT\left\{\bar{v}(nT_s)\right\} = \frac{1}{N_s}\sum_{n=0}^{N_s-1} \bar{v}(nT_s)\, e^{-j2\pi kn/N_s} \tag{7}$$

Notice that, according to (5), the complex coefficients V_k given by (7) must be evaluated for both positive and negative k values, i.e., the bilateral frequency spectrum of $\bar{v}(t)$ must be evaluated.

Let us consider now the impact of additive noise on the evaluation of the coefficients V_k through the DFT (7). In case the time-domain phase voltages v_a, v_b, v_c are corrupted by additive zero-mean identically-distributed white noise:

$$v_{an} = v_a + n_a, \quad v_{bn} = v_b + n_b, \; v_{cn} = v_c + n_c \tag{8}$$

with variance σ_n^2, from (2) we obtain:

$$\bar{v}(t) = v_\alpha + n_\alpha + j\left(v_\beta + n_\beta\right) \tag{9}$$

where

$$n_\alpha = \sqrt{\frac{2}{3}}\left(n_a - \frac{1}{2}(n_b + n_c)\right) \tag{10}$$

$$n_\beta = \frac{1}{\sqrt{2}}(n_b - n_c) \tag{11}$$

Thus, n_α and n_β are zero-mean uncorrelated white noise with variance [28]:

$$\sigma_\alpha^2 = \sigma_\beta^2 = \sigma_n^2 \tag{12}$$

Therefore, the space vector is corrupted by additive noise with the same characteristics as the additive noise corrupting the phase voltages. This point allows the use of well-established results concerning the impact of additive noise on the DFT coefficients provided by (7). Thus, a noisy space vector corrupted by additive zero-mean white noise with variance σ_n^2 results in random DFT coefficients where, from the Central Limit Theorem [28], the real and the imaginary parts are Gaussian, uncorrelated, unbiased random variables with equal variance given by [29], [30]:

$$\sigma^2 = \frac{1}{N_s}\sigma_n^2. \tag{13}$$

This is the fundamental result that will be exploited in the next Sections to derive the probability density functions of the ellipse parameters generated by a noisy three-phase system.

III. ELLIPSE PARAMETERS FOR VOLTAGE SAG ANALYSIS

Voltage sags in three-phase systems can be effectively characterized in terms of the parameters of the elliptical trajectory described by the fundamental frequency component (i.e., the component located at f_0) of the voltage space vector. In fact, under sinusoidal steady-state conditions the space vector (3) describes an ellipse on the complex plane, characterized by the following parameters [11]:

$$r_m = \left|\left|V_p\right| - \left|V_n^*\right|\right| \tag{14}$$

$$r_M = \left|V_p\right| + \left|V_n^*\right| \tag{15}$$

$$\varphi = \frac{1}{2}\left(arg\left(V_p\right) + arg\left(V_n^*\right)\right) \tag{16}$$

where $|\cdot|$ denotes the magnitude, r_m and r_M are the semi-minor and semi-major ellipse axes, respectively, and φ is the ellipse inclination angle. Notice that in (16) the difference between the two phasor arguments would be considered, instead of the sum, if the negative-sequence phasor was not conjugated.

Under ideal conditions, the negative-sequence phasor is equal to zero, and the corresponding space-vector trajectory is a circle with radius $\left|V_p\right|$. A circle, with reduced radius with respect to the nominal voltage, is obtained also in case of balanced faults of the three phases.

In case of unbalanced faults, however (i.e., faults involving only one or two phases), the corresponding negative-sequence component $|V_n| > 0$ yields an elliptical trajectory of the space vector (see Fig. 1). A proper parameter able to detect the elliptical shape of the trajectory is the so-called Shape Index (SI) defined as [11]–[20]:

$$SI = \frac{r_m}{r_M} = \frac{\left|\left|V_p\right| - \left|V_n^*\right|\right|}{\left|V_p\right| + \left|V_n^*\right|} = \frac{\left|1 - \frac{|V_n^*|}{|V_p|}\right|}{1 + \frac{|V_n^*|}{|V_p|}} \tag{17}$$

By taking into account the types of possible voltage sags, and by considering that a voltage sag is defined as a decrease between 10% and 90% of the nominal voltage, in [11]–[20] the threshold level $SI = 0.933$ was calculated. Thus, the condition $SI < 0.933$ detects an unbalanced fault, and the ellipse inclination angle φ provides the type of unbalanced fault according to Fig. 2 where single-phase sags are denoted with S, double-phase sags with D, and the subscripts denote the dropped phases [11]. Inclination angles in Fig. 2 are integer multiples of 30°. Thus, each type of sag is characterized by one of the angles in Fig. 2 with uncertainty ±15°. For example, a single-phase voltage dip involving phase a (i.e., S_a) is characterized by $\varphi = 90° \pm 15°$.

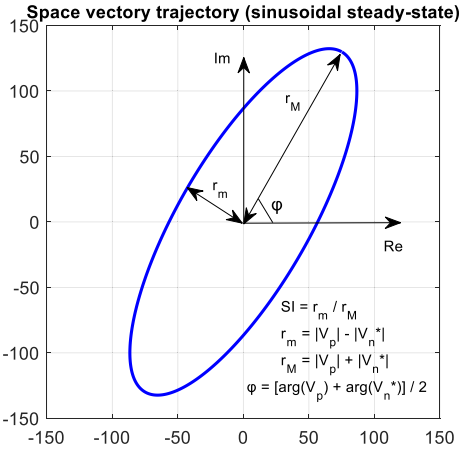

FIGURE 1. Elliptical trajectory of the space vector on the complex plane in case of unbalanced voltage sag. The ellipse parameters are also reported in the figure.

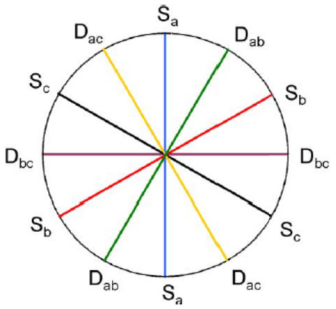

FIGURE 2. Ellipse inclination angles for each type of unbalanced dip (i.e., S for single-phase and D for double-phase dips) [11]. The angles are located at integer multiples of 30°. Therefore, each type of dip is characterized by an inclination angle within the range n30°±15°. For example, single-phase dip on phase *a* (i.e., S_a) is characterized by inclination angle within 90°±15°.

As far as noisy and distorted voltage waveforms are considered, pre-processing is needed in order to extract the positive and negative-sequence phasors at the fundamental frequency. To this aim, the procedure outlined in Section II based on the DFT can be effectively used to discard harmonic waveform components, but additive noise has still impact on magnitude and phase of V_p and V_n^* at $\pm f_0$. Of course, as a general principle, noise impact is larger for spectral components with smaller magnitude. In the present case, it is expected that additive noise has large impact around the threshold condition for SI where the negative-sequence phasor is much smaller in magnitude with respect to the positive-sequence phasor. In fact, at the threshold level $SI = 0.933$, from (17) we have $|V_n^*| / |V_p| \cong 0.035$. Thus, it is expected that additive noise has significant impact in the detection of unbalanced faults (i.e., the condition $SI < 0.933$), since a large impact is expected on the small-magnitude negative-sequence phasor. Moreover, once an unbalanced fault is detected, the inclination angle (16) of the ellipse can be greatly affected by additive noise since a significant impact is expected also on the argument of the small-magnitude negative-sequence phasor.

In the next Section the impact of additive noise on ellipse shape index and inclination angle will be analyzed by deriving the probability density function (PDF) and the main statistical moments of such parameters in terms of the noise variance.

IV. STATISTICAL ANALYSIS OF ADDITIVE NOISE EFFECTS

The ellipse shape index SI (17) and inclination angle φ (16) can be evaluated from the positive-sequence and the negative-sequence phasors V_p and V_n^* through the DFT of the space vector as shown in Section II. Since the space vector is corrupted by additive zero-mean white noise with variance σ_n^2 (see (9)-(12)) the sequence phasors V_p and V_n^* can be treated as complex unbiased random variables, whose real and imaginary parts have Gaussian distribution with variance (13). For the sake of simplicity, a more compact notation will be used:

$$X = V_p = X_r + jX_i \tag{18}$$

$$Y = V_n^* = Y_r + jY_i \tag{19}$$

where the subscripts denote the real and the imaginary parts. In (17) the absolute values of (18)-(19) are required, i.e.:

$$x = |X| = \sqrt{X_r^2 + X_i^2} \tag{20}$$

$$y = |Y| = \sqrt{Y_r^2 + Y_i^2} \tag{21}$$

Therefore, the objective of the statistical analysis can be reformulated as the PDF of the two functions of random variables:

$$SI = \frac{1 - \frac{y}{x}}{1 + \frac{y}{x}} \tag{22}$$

$$\varphi = \frac{1}{2}\left[arctan\left(\frac{X_i}{X_r}\right) + arctan\left(\frac{Y_i}{Y_r}\right)\right] \tag{23}$$

As mentioned above, the largest noise impact is expected for small values of y, i.e., for SI around its threshold limit 0.933 where $y \ll x$. Thus, a reasonable approximation is treating only y as a random variable, while x is treated as a noise-free variable $x = x_0 = \sqrt{X_{0r}^2 + X_{0i}^2}$ (where the subscript 0 denotes the deterministic values corresponding to zero additive noise). Therefore, (22)-(23) can be rewritten as:

$$SI \cong \frac{1 - \frac{y}{x_0}}{1 + \frac{y}{x_0}} \tag{24}$$

$$\varphi \cong \frac{1}{2}\left[arctan\left(\frac{X_{0i}}{X_{0r}}\right) + arctan\left(\frac{Y_i}{Y_r}\right)\right] \tag{25}$$

The validity of the approximations in (24)-(25) will be numerically assessed in Section V.

A. ELLIPSE SHAPE INDEX

1) PROBABILITY DENSITY FUNCTION

The PDF of the ellipse shape index given by (24) can be obtained by resorting to the theorem on transformation of random variables [28]. The starting point is the Gaussian distribution with variance (13) of the unbiased random variables

Y_r and Y_i. From (21) we obtain that the magnitude y has a Rice PDF [28]–[30]:

$$p_y(y) = \frac{y}{\sigma^2} exp\left(-\frac{y_0^2+y^2}{2\sigma^2}\right) I_0\left(\frac{y_0 y}{\sigma^2}\right) \tag{26}$$

where y_0 is the noise-free value of y, and I_0 is the modified Bessel function of the first kind.

In (24) the random variable y is divided by the constant x_0. Thus, the PDF of the new random variable $u = y/x_0$ is given by:

$$p_u(u) = x_0 p_y(x_0 u) = \frac{x_0^2 u}{\sigma^2} exp\left(-\frac{y_0^2 + x_0^2 u^2}{2\sigma^2}\right) I_0\left(\frac{y_0 x_0 u}{\sigma^2}\right) \tag{27}$$

Therefore, the transformation (24) can be written as:

$$z(u) = \frac{1-u}{1+u} \tag{28}$$

where z denotes the random variable SI. To the aim of obtaining the PDF of z, the first derivative and the inversion formula of (28) are needed:

$$z'(u) = \frac{dz}{du} = \frac{-2}{(1+u)^2} \tag{29}$$

$$u(z) = \frac{1-z}{1+z} \tag{30}$$

Therefore, from the theorem on transformation of random variables the PDF of the ellipse shape index can be obtained:

$$p_{SI}(z) = \frac{p_u(u(z))}{|z'(u(z))|} = \frac{2}{(1+z)^2} p_u\left(\frac{1-z}{1+z}\right) \tag{31}$$

The Cumulative Distribution Function (CDF) of the ellipse shape index can be also obtained with a similar procedure. Starting from the CDF of the Rice random variable y:

$$P_y(y) = 1 - Q_1\left(\frac{y_0}{\sigma}, \frac{y}{\sigma}\right) \tag{32}$$

where Q_1 is the first-order Marcum Q-function, the CDF of the scaled random variable $u = y/x_0$ can be readily obtained:

$$P_u(u) = P_y(x_0 u) = 1 - Q_1\left(\frac{y_0}{\sigma}, \frac{x_0 u}{\sigma}\right) \tag{33}$$

By considering the transformation (28) we have that

$$\frac{1-u}{1+u} < z \tag{34}$$

when

$$u > \frac{1-z}{1+z} \tag{35}$$

Therefore, the CDF of the ellipse shape index is given by:

$$P_{SI}(z) = 1 - P_u\left(\frac{1-z}{1+z}\right) = Q_1\left(\frac{y_0}{\sigma}, \frac{x_0}{\sigma}\frac{1-z}{1+z}\right) \tag{36}$$

This result is crucial since, by definition, (36) provides the probability that the ellipse shape index is smaller than a given level z (e.g., the SI threshold level). By denoting as SI_0 the noise-free value of the shape index (24), i.e.:

$$SI_0 = \frac{1 - \frac{y_0}{x_0}}{1 + \frac{y_0}{x_0}} \tag{37}$$

x_0 in (36) can be expressed as:

$$x_0 = y_0 \frac{1+SI_0}{1-SI_0} \tag{38}$$

Thus, by considering the threshold value $z_T = 0.933$ for voltage sag detection, from (36) we obtain the detection probability:

$$P_D = Q_1\left(SNR, SNR\frac{1+SI_0}{1-SI_0}\frac{1-z_T}{1+z_T}\right) \tag{39}$$

where the signal-to-noise ratio (SNR) is defined as:

$$\text{SNR} = \frac{y_0}{\sigma} \tag{40}$$

Finally, for the sake of completeness, the more general case where the assumption $y \ll x$ is not met can be considered. In this case, the random variable $u = y/x$ is not a simple scaled version of y, but it is the ratio between two random variables with Rice distribution and equal variance. The PDF of such ratio is given by [31]:

$$\begin{aligned} p_u(u) = {} & \frac{2u}{(1+u^2)^2} exp\left(-\frac{y_0^2 + x_0^2 u^2}{2\sigma^2(1+u^2)}\right) \\ & \times \left[\left(1 + \frac{x_0^2 + y_0^2 u^2}{2\sigma^2(1+u^2)}\right) I_0\left(\frac{y_0 x_0 u}{\sigma^2(1+u^2)}\right)\right. \\ & \left. + \left(\frac{y_0 x_0 u}{\sigma^2(1+u^2)}\right) I_1\left(\frac{y_0 x_0 u}{\sigma^2(1+u^2)}\right)\right] \end{aligned} \tag{41}$$

The numerical convergence of the PDF (41) is more critical than (27) as the ratio $x_0 y_0/\sigma^2$ increases.

The CDF of the random variable $u = y/x$ is given by [31]:

$$P_u(u) = Q_1(A, B) - \left(\frac{\sigma A}{x_0 u}\right)^2 exp\left(-\frac{A^2+B^2}{2}\right) I_0(AB) \tag{42}$$

where:

$$A = \frac{x_0 u}{\sigma\sqrt{1+u^2}}, \quad B = \frac{y_0}{\sigma\sqrt{1+u^2}} \tag{43}$$

Equations (41) and (42) can be used in (31) and (36) to obtain the general expressions for the PDF and CDF of the shape index SI without the restriction $y \ll x$.

2) MEAN VALUE AND VARIANCE

Approximate expressions for the mean value and the variance of the ellipse shape index can be obtained by resorting to the Taylor expansion approach [28]. To this aim, the first and second order derivatives of the transformation (28) are needed. The first order derivative is given by (29), whereas the second order derivative is given by:

$$z''(u) = \frac{4}{(1+u)^3} \tag{44}$$

Thus, the approximate mean value of the ellipse shape index is given by:

$$\mu_{SI} \cong z(\mu_u) + \frac{1}{2} z''(\mu_u)\sigma_u^2 = \frac{1-\mu_u}{1+\mu_u} + \frac{2}{(1+\mu_u)^3}\sigma_u^2 \quad (45)$$

where μ_u and σ_u^2 can be readily expressed in terms of μ_y and σ_y^2 (i.e., the well-known mean value and variance of a Rice distribution) [32]:

$$\mu_u = \frac{1}{x_0}\mu_y = \frac{1}{x_0}\sigma\sqrt{\frac{\pi}{2}} L_{1/2}\left(-\frac{y_0^2}{2\sigma^2}\right) \quad (46)$$

$$\sigma_u^2 = \frac{1}{x_0^2}\sigma_y^2 = \frac{1}{x_0^2}\left(2\sigma^2 + y_0^2 - \frac{\pi\sigma^2}{2} L_{1/2}^2\left(-\frac{y_0^2}{2\sigma^2}\right)\right) \quad (47)$$

where L is the Laguerre polynomial.

The approximate variance of the ellipse shape index is given by [28]:

$$\sigma_{SI}^2 \cong \left(z'(\mu_u)\right)^2 \sigma_u^2 = \frac{4}{(1+\mu_u)^4}\sigma_u^2 \quad (48)$$

where μ_u and σ_u^2 are given by (46)-(47).

B. ELLIPSE INCLINATION ANGLE

1) PROBABILITY DENSITY FUNCTION

From (25) the first step in order to obtain the PDF of the inclination angle φ is the analysis of the random variable $w = Y_i/Y_r$. The PDF of the ratio of two Gaussian random variables with equal variance is given by [31]:

$$p_w(w) = \frac{1}{\pi\left(1+w^2\right)} exp\left(-\frac{y_0^2}{2\sigma^2}\right) + \frac{Y_{0r} + Y_{0i}w}{\sigma\sqrt{2\pi}\left(1+w^2\right)^{3/2}} exp\left(-\frac{(Y_{0i} - Y_{0r}w)^2}{2\sigma^2\left(1+w^2\right)}\right) \times \left[1 - erfc\left(\frac{Y_{0r} + Y_{0i}\frac{w}{\sqrt{2}}}{\sigma\sqrt{1+\frac{1}{2}w^2}}\right)\right] \quad (49)$$

where Y_{0r} and Y_{0i} are the noise-free values of Y_r and Y_i, respectively, and *erfc* is the complementary error function.

According to (25) the following transformation of random variable must be solved:

$$g(w) = \frac{1}{2}\left(\varphi_{X_0} + \arctan(w)\right) \quad (50)$$

Similarly to the shape index case, the first derivative and the inversion formula of (50) are needed:

$$g'(w) = \frac{dg}{dw} = \frac{1}{2}\frac{1}{1+w^2} \quad (51)$$

$$w(g) = \tan(2g - \varphi_{X_0}) \quad (52)$$

Thus, according to the theorem on the transformation of random variables the PDF of the ellipse inclination angle is given by:

$$p_\varphi(g) = \frac{p_w(w(g))}{|g'(w(g))|} = 2\left(1 + tan^2(2g - \varphi_{X_0})\right) p_w\left(\tan(2g - \varphi_{X_0})\right) \quad (53)$$

Notice that (53) provides the PDF of the inclination angles expressed in radians. The PDF for inclination angles in degrees is given by:

$$p_{\varphi_d}(g_d) = \frac{\pi}{180} p_\varphi\left(\frac{\pi}{180} g_d\right) \quad (54)$$

where $g_d = g \cdot 180/\pi$.

The CDF of the inclination angle can be obtained by numerical integration of the PDF (53)-(54).

2) MEAN VALUE AND VARIANCE

Approximate expressions for the mean value and the variance of the ellipse inclination angle can be obtained by using the Taylor expansion of (25) with respect to the two Gaussian random variables Y_r and Y_i [28]. Thus, the mean value of φ is given by:

$$\mu_\varphi \cong \frac{1}{2}\left[arctan\left(\frac{X_{0i}}{X_{0r}}\right) + arctan\left(\frac{Y_{0i}}{Y_{0r}}\right)\right] = \varphi_0 \quad (55)$$

where the correction term related to the second-order partial derivatives is not present since it is null. Therefore, the inclination angle is a random variable with negligible bias.

The variance of the inclination angle can be estimated through the first-order partial derivatives:

$$\sigma_\varphi^2 \cong \left(\frac{\partial\varphi}{\partial Y_r}\right)^2 \sigma^2 + \left(\frac{\partial\varphi}{\partial Y_i}\right)^2 \sigma^2 = \frac{1}{4y_0^2}\sigma^2 = \frac{1}{4SNR^2} \quad (56)$$

Notice that since σ_φ^2 is a function of the *SNR* only, it is not dependent on the nominal shape index SI_0.

Finally, it is worth noticing that by removing the assumption $y \ll x$, i.e., by treating also X_i/X_r as a random variable in (23), the inclination angle φ would be given by the weighted sum of the two random variables $\arctan(X_i/X_r)$ and $\arctan(Y_i/Y_r)$. Thus, the PDF of φ would be given by the convolution of two PDFs [28]. A closed-form analytical result is not available in the literature. Therefore, the analytical results derived in this Subsection are limited to the assumption $y \ll x$. Numerical simulations, however, will prove that such assumption leads to reasonably accurate results.

V. NUMERICAL VALIDATION

The analytical results derived in Section IV were validated by means of numerical simulations in Matlab. The simulation process was implemented according to the following steps. First, the noise-free values of the positive and negative-sequence phasors V_p and V_n were selected in order to set the noise-free value SI_0 of the ellipse shape index (37), and the noise-free value φ_0 of the ellipse inclination angle (55). Second, by inversion of the symmetrical component transformation (4) (with null zero-sequence component) the phasors of the phase voltages V_a, V_b, V_c were calculated. Then, the corresponding time-domain voltages $v_a(t)$, $v_b(t)$, $v_c(t)$ were obtained by assuming fundamental frequency $f_0 = 50Hz$. Each time-domain waveform was corrupted by additive zero-mean Gaussian noise with variance σ_n^2. Such variance was selected according to the desired value of the *SNR* (40), where

σ is related to σ_n through (13). The three noisy waveforms were sampled by taking $N_s = 256$ samples per period, i.e., with sampling frequency $f_s = N_s f_0 = 12.8kHz$. Then, according to (2), the three waveforms where combined to define the voltage space vector, and the time-to-frequency transformation of the space vector (i.e., the DFT (7)) was calculated through the Fast Fourier Transform. The time window was one period in length (i.e., the number of processed samples was N_s). Therefore, the DFT frequency resolution was $\Delta f = f_s/N_s = 50Hz$. Thus, according to (7), the obtained frequency coefficients V_1 and V_{-1} were the estimates of V_p and V_n^*, respectively. The ratio $|V_{-1}|\,/\,|V_1|$, and the arguments of V_1 and V_{-1} were used to evaluate the shape index (17) and the inclination angle (16). Such evaluations were repeated N times (with $N \geq 10^4$) by generating new sequences of random noise added to the time-domain waveforms $v_a(t)$, $v_b(t)$, $v_c(t)$. Thus, for each selection of the parameters SI_0, φ_0, and SNR, a set of N realizations of the random variables SI and φ were calculated. Therefore, the statistical properties of SI and φ, i.e., PDF, CDF, mean value and variance, were numerically evaluated and compared with the corresponding analytical results obtained in Section IV.

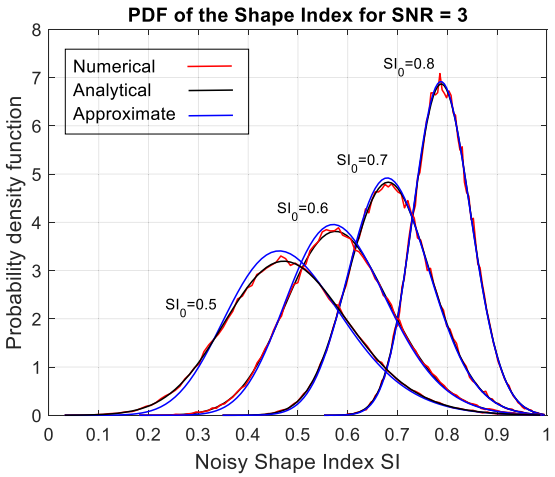

FIGURE 3. Probability density function of the ellipse shape index for different values of the noise-free shape index SI_0. Numerical results (red lines) are compared with analytical complete (black lines) and approximate (blue lines) results.

Fig. 3 shows the PDF of the shape index SI with $SNR = 3$. Four different values of the noise-free shape index SI_0 were selected, i.e., 0.5, 0.6, 0.7, and 0.8. Numerical results obtained through the simulation procedure outlined above are represented by the red lines. The approximate analytical PDF given by (27) substituted into (31) is represented by blue lines, whereas the general analytical PDF given by (41) substituted into (31) is represented by black lines. The objective of this figure is showing that by increasing SI_0 the approximate analytical PDF (blue lines) provides satisfactory results. Since we are interested in the case of SI_0 approaching the limiting value 0.933, the approximate analytical PDF can be effectively used. Thus, in the next figures, only the approximate analytical PDF will be represented.

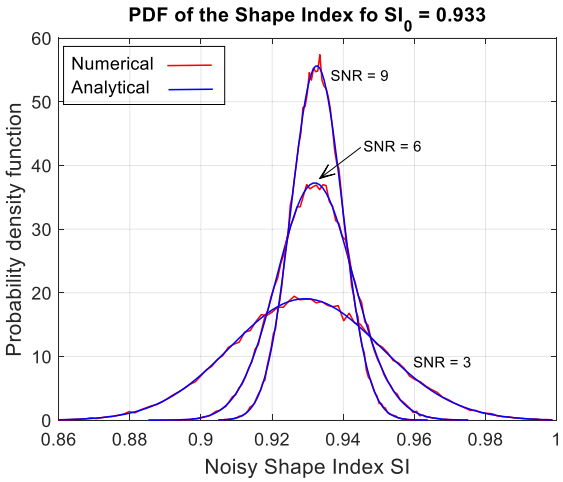

FIGURE 4. Probability density function of the ellipse shape index for different values of the signal-to-noise ratio SNR. Numerical results (red lines) are compared with analytical results (blue lines).

Fig. 4 shows the behavior of the PDF of the shape index with $SI_0 = 0.933$, and for three different SNR values, i.e., 3, 6, and 9. By increasing the SNR (i.e., by decreasing the noise level) the spread of the PDF decreases. Notice that even for $SNR = 9$ the shape index can take values around 0.96, i.e., well above the threshold value 0.933 used to detect a voltage sag. For $SNR = 3$ the shape index can take values even around 1, that is the case where the ellipse becomes a circle. This is consistent with the fact that $SNR = 3$ means $y_0 = 3\sigma$. Thus, the noisy y can take values even close to zero.

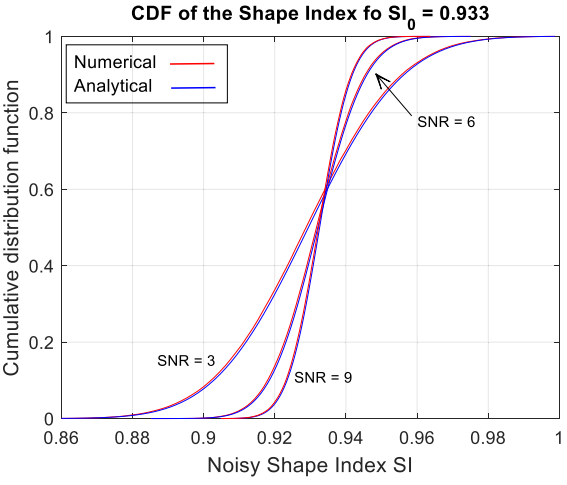

FIGURE 5. Cumulative distribution function of the ellipse shape index for different values of the signal-to-noise ratio SNR. Numerical results (red lines) are compared with analytical results (blue lines).

Fig. 5 shows the CDF of the shape index corresponding to the PDF shown in Fig. 4. The blue lines represent the analytical CDF given by (36). The slope of the central part of the CDF increases with SNR. In fact, by decreasing the noise level to zero the CDF approaches a discontinuous behavior at 0.933.

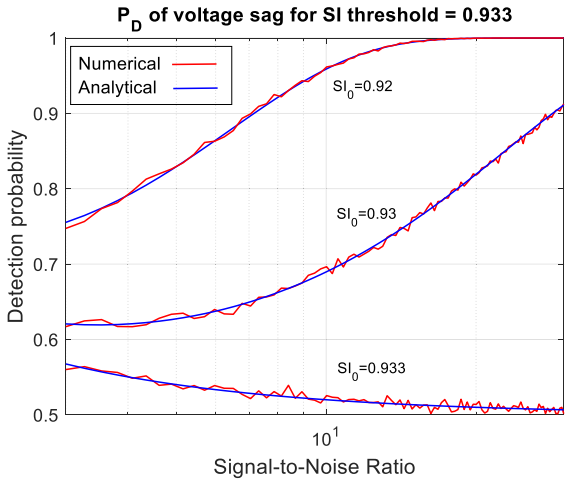

FIGURE 6. Detection probability of the ellipse shape index for different values of the noise-free shape index SI_0. Numerical results (red lines) are compared with analytical results (blue lines).

Fig. 6 shows the detection probability (39) of a voltage sag, i.e., the probability that the shape index is lower than the threshold 0.933, for three different values of SI_0, i.e., 0.933, 0.93, and 0.92. For $SI_0 = 0.933$, by increasing the *SNR* the PDF peak approaches the location 0.933 (see Fig. 4). Thus, the detection probability approaches 0.50 for increasing *SNR*. For $SI_0 = 0.93$ and $SI_0 = 0.92$, however, the location of the PDF peak is lower than 0.933. Thus, by increasing *SNR* the PDF shrinks and the detection probability approaches 1.

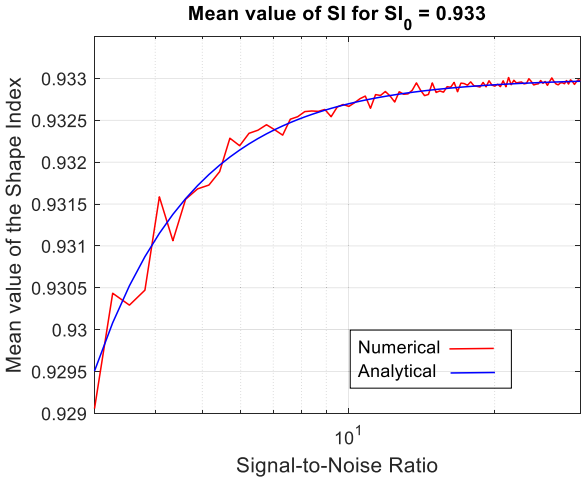

FIGURE 7. Mean value of the ellipse shape index for noise-free shape index $SI_0 = 0.933$ as a function of the signal-to-noise ratio *SNR*. Numerical results (red lines) are compared with analytical results (blue lines).

Fig. 7 shows the mean value (45) of the shape index, with $SI_0 = 0.933$, as a function of the *SNR*. The mean value approaches SI_0 as *SNR* increases. This behavior corresponds to the shift of the PDF peak in Fig. 4 as *SNR* increases. Similar curves can be obtained for different values of SI_0.

Fig. 8 shows the behavior of the standard deviation of the shape index (i.e., the square root of (48)) as a function of

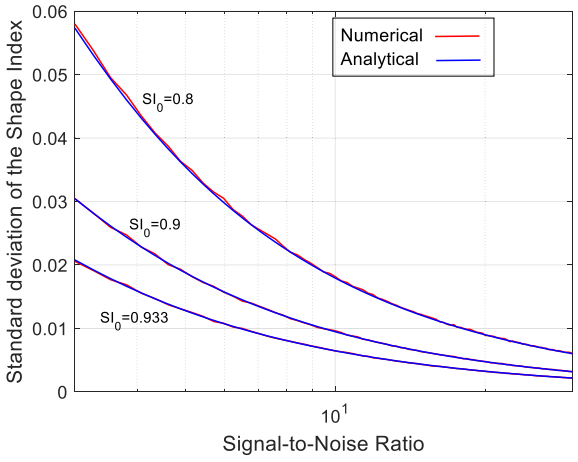

FIGURE 8. Standard deviation of the ellipse shape index for noise-free shape index $SI_0 = 0.933, 0.9, 0.8$, as a function of the signal-to-noise ratio *SNR*. Numerical results (red lines) are compared with analytical results (blue lines).

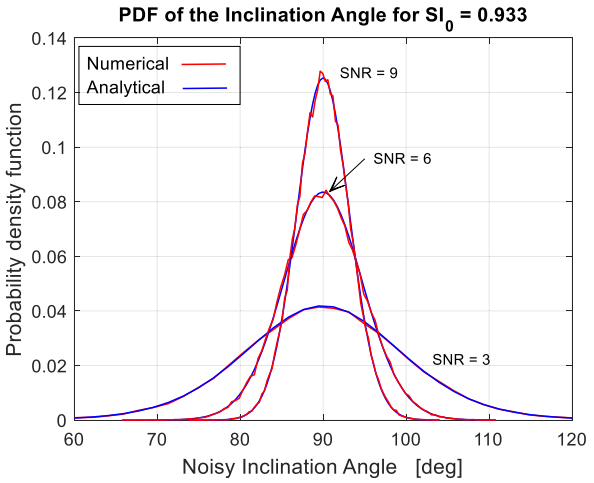

FIGURE 9. Probability density function of the ellipse inclination angle for different values of the signal-to-noise ratio *SNR*. Numerical results (red lines) are compared with analytical results (blue lines).

SNR, for three different values of SI_0, i.e., 0.933, 0.9, 0.8. This figure can be compared with Fig. 3 where it is shown that, for a given *SNR* value, the standard deviation increases for decreasing SI_0. This is because both y_0 and σ increase to keep *SNR* constant.

Fig. 9 shows the behavior of the PDF (54) of the ellipse inclination angle with $SI_0 = 0.933$ and for three different values of *SNR*, i.e., 3, 6, and 9. The selected phases for V_p and V_n^* were such that the noise-free inclination angle was $\varphi_0 = 90°$. Notice that even for $SNR = 9$ the spread of the PDF is about $\pm 10°$. This is a crucial point since from Fig. 2 each type of voltage sag can be identified within an angular range $\pm 15°$ due to circuit parameters. Therefore, the impact of noise could result in a wrong identification of the type of voltage sag. Of course, this potential problem is emphasized for smaller *SNR* values. For example, $SNR = 6$ corresponds to an approximate PDF spread $\pm 15°$, i.e., the same angular range of each sector in Fig. 2.

Finally, Fig. 10 shows the behavior of the standard deviation of the inclination angle (i.e., the square root of (56)). As already pointed out, σ_φ is a function of the *SNR* only (in the approximate result (56)). Thus, the behavior shown in Fig. 10 is valid independently of SI_0. Notice that, since the PDF in Fig. 9 are approximately Gaussian, the PDF spread is approximately $\pm 3\sigma_\varphi$, where σ_φ can be read in Fig. 10.

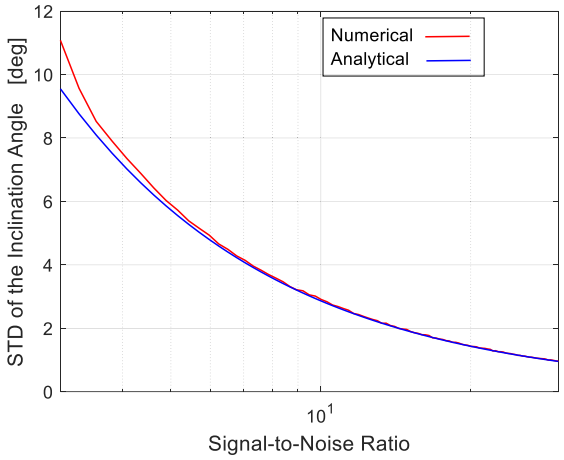

FIGURE 10. Standard deviation of the ellipse inclination angle as a function of the signal-to-noise ratio *SNR*. Numerical results (red lines) are compared with analytical results (blue lines).

VI. VALIDATION WITH REAL DATA

Real data recorded by DOE/EPRI [33] were used for further validation of the analytical results derived in the paper. In particular, the event number 0243 was considered. According to [33] the fault was due to a tree fallen on phase a.

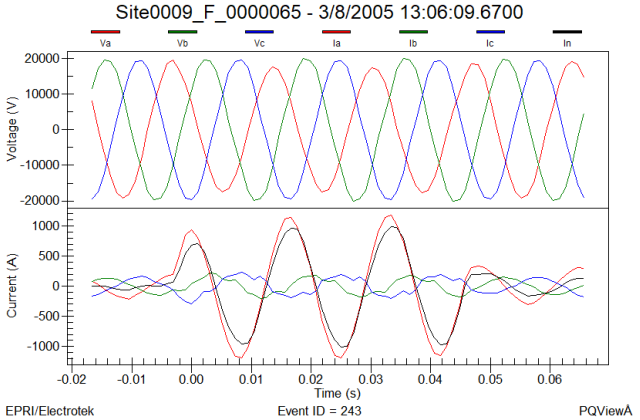

FIGURE 11. Real data voltages and currents recorded by DOE/EPRI, event number 0243 due to a tree fallen on phase *a* [33].

Fig. 11 shows the time-domain behavior of voltages and currents within a time window consisting in five periods (fundamental frequency $f_0 = 60Hz$). A small decrease in the magnitude of voltage a (red line) can be observed in the central part of the time window. Waveforms were monitored by taking $N_s = 16$ samples per period. A small number of samples per period can be advantageous since real-time continuous monitoring is needed.

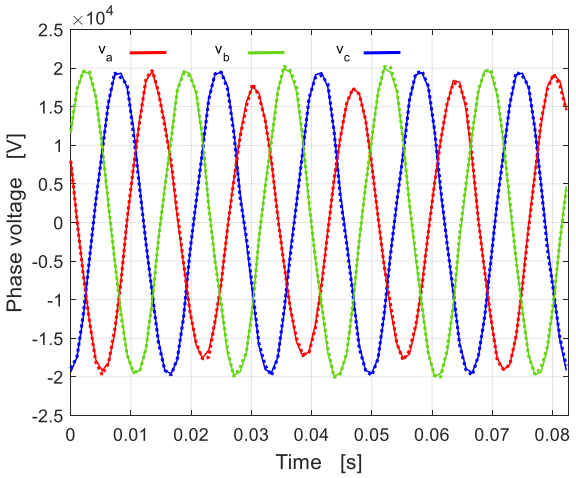

FIGURE 12. Voltage waveforms in Fig. 11 (solid lines) corrupted by additive zero-mean Gaussian noise with standard deviation $\sigma_n = 320V$ (dashed lines).

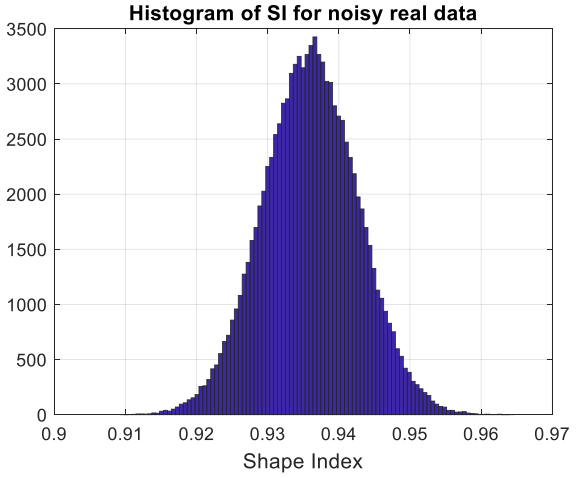

FIGURE 13. Histogram of ellipse shape index for the noisy voltages in Fig. 12 ($N = 10^5$ repeated runs).

The procedure based on the DFT described in this paper was used to evaluate the voltage ellipse shape index *SI* and inclination angle φ in each period. The shape index takes its minimum value 0.9364 at the third period, and the corresponding inclination angle is 77.5° (i.e., within the range 90° ± 15° characteristic of a grounded phase a). Notice that, according to the choice of a threshold level equal to 0.933, the voltage sag would not be detected. Additive noise, however, is always present in measured waveforms. Unfortunately, estimate of additive noise level in Fig. 11 is a hard task since the underlying signal is non-stationary. For comparison purposes only, we can for example consider the case of additive noise with $SNR = 9$, already considered in Sections IV and V. From the DFT analysis of the third period of the space vector, we obtain that $|V_{-1}| = |V_n^*| \cong 750V$. Thus, from (40) the corresponding frequency-domain standard deviation is given by $\sigma \cong 80V$. From (13), for

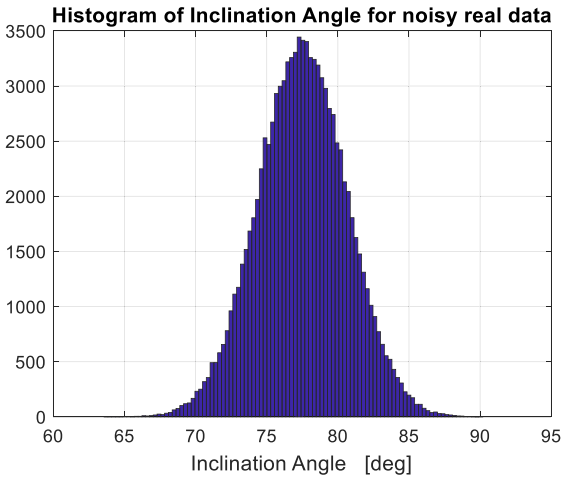

FIGURE 14. Histogram of ellipse inclination angle for the noisy voltages in Fig. 12 ($N = 10^5$ repeated runs).

time-domain noise we obtain $\sigma_n = \sigma\sqrt{N_s} \cong 320V$. Notice that a small number of samples per period results in low-level time-domain noise. Actually, σ_n must be compared with the RMS value of the phase voltages, i.e., $V_{rms} \cong \frac{20}{\sqrt{2}}kV \cong 14kV$. Therefore, since the ratio $V_{rms}/\sigma_n \cong 44$, the effect of time-domain additive noise cannot be clearly observed on the waveform amplitude. Fig. 12 shows an example of the three voltage waveforms corrupted by additive zero-mean Gaussian noise with $\sigma_n = \sigma\sqrt{N_s}$ (dashed lines). Thus, the time-domain effect of such noise level seems negligible in the time-domain. However, in Section IV and V it was shown that such noise level can produce significant deviations of the shape index and the inclination angle. To illustrate this point, and for further validation of the analytical results, a repeated run analysis (with $N = 10^5$) was performed by adding zero-mean Gaussian noise with variance σ_n^2 to the three voltage waveforms in Fig. 11. The distribution of the shape index and the inclination angle are represented by the histograms in Figs. 13 and 14, respectively. The range of the histogram in Fig. 13 (i.e., $0.91 \div 0.96$) is approximately the same range of the PDF with $SNR = 9$ in Fig. 4. Thus, noise effect can result in either detection or no-detection of the voltage sag. The range of the histogram in Fig. 14 (i.e., $\Delta\varphi \cong 20°$) is approximately the same range of the PDF with $SNR = 9$ in Fig. 9, with different mean value because this is a function of circuit parameters. Notice that noise effect can result in inclination angle outside the characteristic range $90° \pm 15°$, producing a wrong identification of the voltage sag type.

VII. CONCLUSION AND DISCUSSION

In this Section, the main achievements obtained in the paper are summarized and discussed.

The parameters of the elliptical trajectory (i.e., shape index and inclination angle) of a voltage space vector on the complex plane at power frequency are widely used to detect and classify three-phase voltage sags. In real applications, however, the voltage space vector is corrupted by harmonics and additive noise. Therefore, since the ellipse parameters refer to the power frequency component only, pre-processing of space vector is required.

Within the context of power system analysis, the most common technique for harmonic analysis is the well-known DFT. It is worth noticing that, for the present analysis, the DFT was used only to measure the power frequency components of the voltage space vector, i.e., the positive-sequence and the negative-sequence components at power frequency. Thus, since the ellipse parameters depend only on the power frequency components, the DFT is used only to isolate the power frequency components with respect to the harmonic content. Moreover, in the paper it was assumed that sampling was synchronized with voltage fundamental frequency. In practice this condition can be achieved by using a closed-loop measuring system. Indeed, in case of lack of synchronization, windowing of voltage samples (e.g., Hann window) is required to minimize spectral leakage. In this case the analytical results derived in the paper hold provided that the variance (13) is multiplied by the equivalent noise bandwidth (*ENBW*) of the selected window (e.g., $ENBW = 1.50$ for the Hann window) [29].

Once the power frequency components of the voltage space vector are measured, the impact of additive noise on the corresponding DFT coefficients must be evaluated since such coefficients are used to calculate the ellipse parameters. Under weak assumptions, regardless the specific distribution of additive noise, the Central Limit Theorem guarantees that the real and imaginary parts of DFT coefficients can be approximated as uncorrelated and unbiased Gaussian random variables. This is the fundamental starting point of the analytical derivations presented in the paper. In fact, from this point, the statistical properties of the ellipse parameters were derived in analytical form. In particular, the PDF, the CDF, the mean value, and the variance of the ellipse shape index and inclination angle were derived as functions of the additive noise variance. These results allow a complete statistical characterization of the ellipse parameters. To the Author's knowledge, such statistical characterization was still lacking in the relevant literature, and therefore a straightforward comparison with similar results cannot be accomplished. In Section V the analytical results were validated through numerical simulation of the whole measurement process.

The obtained statistical characterization of the ellipse parameters can be useful for two reasons. First, measured ellipse parameters can be characterized in terms of uncertainty. In fact, the analysis proposed in the paper can be regarded as a study of uncertainty propagation. Since ellipse parameters are used to distinguish and classify voltage sags, the corresponding uncertainty levels provide the required information for a proper identification of voltage sag types. Second, voltage sag detection is conventionally characterized by shape index $SI < 0.933$. In case of noisy measurements, the comparison between the measured shape index and the threshold level 0.933 can be evaluated in statistical terms, i.e., in terms of detection probability. To this aim, it is worth

noticing that, according to (17), the threshold $SI = 0.933$ corresponds to voltage unbalance $|V_n^*|/|V_p| \cong 0.035$. Therefore, if a system is working in unbalanced mode (e.g., a distribution system), then the whole methodology based on the space vector can be still used provided that the voltage unbalance is lower that 3.5% [34]. For higher voltage unbalance the whole space-vector approach investigated in [11]–[20] and in this paper requires further investigation.

REFERENCES

[1] R. C. Dugan, S. Santoso, M. F. McGranaghan, and H. W. Beaty, *Electrical Power Systems Quality*, vol. 2. New York, NY, USA: McGraw-Hill, 1996.

[2] M. H. Bollen, "Voltage sags characterization," in *Understanding Power Quality Problems: Voltage Sags and Interruptions*. New York, NY, USA: Wiley-IEEE, 2000, pp. 139–251.

[3] *IEEE Recommended Practice for Monitoring Electric Power Quality*, IEEE Standard 1159-2009 (Revision of IEEE Std 1159-1995), Jun. 2009.

[4] P. Wei, Y. Xu, Y. Wu, and C. Li, "Research on classification of voltage sag sources based on recorded events," *CIRED Open Access Proc. J.*, vol. 2017, no. 1, pp. 846–850, Oct. 2017.

[5] H. Liao, J. V. Milanovic, M. Rodrigues, and A. Shenfield, "Voltage sag estimation in sparsely monitored power systems based on deep learning and system area mapping," *IEEE Trans. Power Del.*, vol. 33, no. 6, pp. 3162–3172, Dec. 2018.

[6] E. Styvaktakis, M. H. J. Bollen, and I. Y. H. Gu, "Expert system for classification and analysis of power system events," *IEEE Trans. Power Del.*, vol. 17, no. 2, pp. 423–428, Apr. 2002.

[7] C. Venkatesh, D. V. S. S. Siva. Sarma, and M. Sydulu, "Classification of voltage sag, swell and harmonics using S-transform based modular neural network," in *Proc. 14th Int. Conf. Harmon. Qual. Power (ICHQP)*, Bergamo, Italy, Sep. 2010, pp. 1–7.

[8] K. M. Silva, B. A. Souza, and N. S. D. Brito, "Fault detection and classification in transmission lines based on wavelet transform and ANN," *IEEE Trans. Power Del.*, vol. 21, no. 4, pp. 2058–2063, Oct. 2006.

[9] P. Janik and T. Lobos, "Automated classification of power-quality disturbances using SVM and RBF networks," *IEEE Trans. Power Del.*, vol. 21, no. 3, pp. 1663–1669, Jul. 2006.

[10] M. Manjula, A. V. R. S. Sarma, and S. Mishra, "Detection and classification of voltage sag causes based on empirical mode decomposition," in *Proc. Annu. IEEE India Conf.*, Hyderabad, India, Dec. 2011, pp. 1–5.

[11] V. Ignatova, P. Granjon, and S. Bacha, "Space vector method for voltage dips and swells analysis," *IEEE Trans. Power Del.*, vol. 24, no. 4, pp. 2054–2061, Oct. 2009.

[12] M. R. Alam, K. M. Muttaqi, and A. Bouzerdoum, "Characterizing voltage sags and swells using three-phase voltage ellipse parameters," *IEEE Trans. Ind. Appl.*, vol. 51, no. 4, pp. 2780–2790, Jul. 2015.

[13] J. R. Camarillo-Penaranda and G. Ramos, "Fault classification and voltage sag parameter computation using voltage ellipses," *IEEE Trans. Ind. Appl.*, vol. 55, no. 1, pp. 92–97, Jan. 2019.

[14] J. R. Camarillo-Penaranda and G. Ramos, "Characterization of voltage sags due to faults in radial systems using three-phase voltage ellipse parameters," *IEEE Trans. Ind. Appl.*, vol. 54, no. 3, pp. 2032–2040, May 2018.

[15] T. García-Sánchez, E. Gómez-Lázaro, E. Muljadi, M. Kessler, and A. Molina-García, "Approach to fitting parameters and clustering for characterising measured voltage dips based on two-dimensional polarisation ellipses," *IET Renew. Power Gener.*, vol. 11, no. 10, pp. 1335–1343, Aug. 2017.

[16] A. Bagheri and M. J. H. Bollen, "Space phasor model based monitoring of voltages in three phase systems," in *Proc. 18th Int. Conf. Harmon. Qual. Power (ICHQP)*, May 2018, pp. 1–6.

[17] S. Li, L. Xie, and Y. Liu, "Fast identification method for voltage sag type and characteristic," in *Proc. 45th Annu. Conf. IEEE Ind. Electron. Soc. (IECON)*, Lisbon, Portugal, Oct. 2019, pp. 3399–3404.

[18] A. Bagheri, M. H. J. Bollen, and I. Y. H. Gu, "Improved characterization of multi-stage voltage dips based on the space phasor model," *Electr. Power Syst. Res.*, vol. 154, p. 319, Jan. 2018.

[19] M. R. Alam, K. M. Muttaqi, and A. Bouzerdoum, "A new approach for classification and characterization of voltage dips and swells using 3-D polarization ellipse parameters," *IEEE Trans. Power Del.*, vol. 30, no. 3, pp. 1344–1353, Jun. 2015.

[20] M. R. Alam, K. M. Muttaqi, and T. K. Saha, "Classification and localization of fault-initiated voltage sags using 3-D polarization ellipse parameters," *IEEE Trans. Power Del.*, vol. 35, no. 4, pp. 1812–1822, Aug. 2020.

[21] B. M. Mahmmod, A. M. Abdul-Hadi, S. H. Abdulhussain, and A. Hussien, "On computational aspects of Krawtchouk polynomials for high orders," *J. Imag.*, vol. 6, no. 8, pp. 1–12, 2020.

[22] A. M. Abdul-Hadi, S. H. Abdulhussain, and B. M. Mahmmod, "On the computational aspects of Charlier polynomials," *Cogent Eng.*, vol. 7, no. 1, pp. 1–21, Jan. 2020.

[23] E. Clarke, *Circuit Analysis of A-C Power Systems*. New York, NY, USA: Wiley, 1943.

[24] J. M. Aller, A. Bueno, and T. Paga, "Power system analysis using space-vector transformation," *IEEE Trans. Power Syst.*, vol. 17, no. 4, pp. 957–965, Nov. 2002.

[25] D. Bellan and G. Superti-Furga, "Space-vector state-equation analysis of three-phase transients," *J. Electr. Syst.*, vol. 14, no. 1, pp. 188–198, 2018.

[26] J. C. Das, *Understanding Symmetrical Components for Power System Modeling*. Hoboken, NJ, USA: Wiley, 2017.

[27] D. Bellan, "On the statistical characterization of the discrete Fourier transform of noisy space vectors," in *Proc. Int. Electr. Eng. Congr. (iEECON)*, Krabi, Thailand, Mar. 2018, pp. 1–4.

[28] A. Papoulis, *Probability Random Variables and Stochastic Processes*. New York, NY, USA: McGraw-Hill, 1991.

[29] D. Bellan, A. Gaggelli, and S. A. Pignari, "Noise effects in time-domain systems involving three-axial field probes for the measurement of nonstationary radiated emissions," *IEEE Trans. Electromagn. Compat.*, vol. 51, no. 2, pp. 192–203, May 2009.

[30] J. Schoukens and J. Renneboog, "Modeling the noise influence on the Fourier coefficients after a discrete Fourier transform," *IEEE Trans. Instrum. Meas.*, vol. IM-35, no. 3, pp. 278–286, Sep. 1986.

[31] M. K. Simon, *Probability Distributions Involving Gaussian Random Variables*. New York, NY, USA: Springer, 2002.

[32] D. Bellan, "On the statistics of noisy space vector in power quality analysis," *Int. J. Eng. Technol.*, vol. 8, no. 5, pp. 2177–2183, Oct. 2016.

[33] *DOE Disturbance Library*, US Dept. Energy Elect. Power Res. Inst., Orlando, FL, USA, 2007. [Online]. Available: http://pqmon.epri.com/disturbance_library/see_all.asp

[34] *Electromagnetic Compatibility (EMC)—Limits—Assessment of Emission Limits for the Connection of Unbalanced Installations to MV, HV and EHV Power Systems*, Standard IEC/TR 61000-3-13, Ed. I, International Electrotechnical Commission, 2008.

DIEGO BELLAN (Member, IEEE) received the M.Sc. and Ph.D. degrees in electrical engineering from the Politecnico di Milano, Milan, Italy, in 1994 and 1999, respectively.

He is currently with the Department of Electronics, Information and Bioengineering, Politecnico di Milano, where he teaches Advanced Circuit Theory. He has published more than 100 papers in international journals and conference proceedings. His research interests include power quality, power system analysis, low-frequency electromagnetic compatibility, and statistical techniques. He was involved in the staff of several funded research projects, concerning EMC in the space sector and in the railway sector, and projects supported by the Italian Ministry of University and Research. He was also the principal investigator of several funded research activities concerning electromagnetic modeling of electromechanical devices. He also serves as a reviewer for IEEE TRANSACTIONS and other international journals. He is also a member of the committees of many international conferences, and delivered several plenary talks and tutorials.